Rim dynamics and droplet ejections upon drop impact on star-shaped poles

Tobias Bauer and Tristan Gilet*

Microfluidics Lab, Department of Aerospace and Mechanical Engineering, University of Liège, Belgium †

(Dated: July 18, 2024)

When a drop impacts next to the edge of a solid substrate, it may spread beyond this edge. It then forms a liquid sheet surrounded by a rim from which droplets may be ejected. This work investigates the influence of the edge shape on the rim dynamics and subsequent droplet ejections. Experiments of drop impacts on star-shaped poles are reported. Both the rim and the ejected droplets are tracked. An analytical model is proposed to rationalize the amplitude of rim deformations induced by the edge shape. Statistical distributions of position, size and velocity of ejected droplets are also shaped by the edge geometry.

I. INTRODUCTION

Vegetation intercepts a significant fraction of rainfalls [1]: many raindrops impact and splash at the surface of leaves, stems, flowers, and branches [2]. This interception completely modifies the raindrop size and momentum distributions. While the size distribution of incoming raindrops is approximately a truncated exponential [3], the size distribution of release throughfall (i.e., rainwater ejected from plant surfaces) is bimodal: it comprises large drips from vegetation elements and small droplets ejected upon splash [4]. Drips may reach the ground with more kinetic energy than any non-intercepted raindrop, which may considerably enhance erosion [5] and runoff [6]. By contrast, drips contribute less to the wash-off of plants in the understory than non-intercepted raindrops [7]. Splash droplets represent an efficient way for many fungal spores to travel between parts of a plant or between neighboring plants [8, 9]. The subsequent dispersal of foliar pathogens has dramatic consequences for many major crops [10].
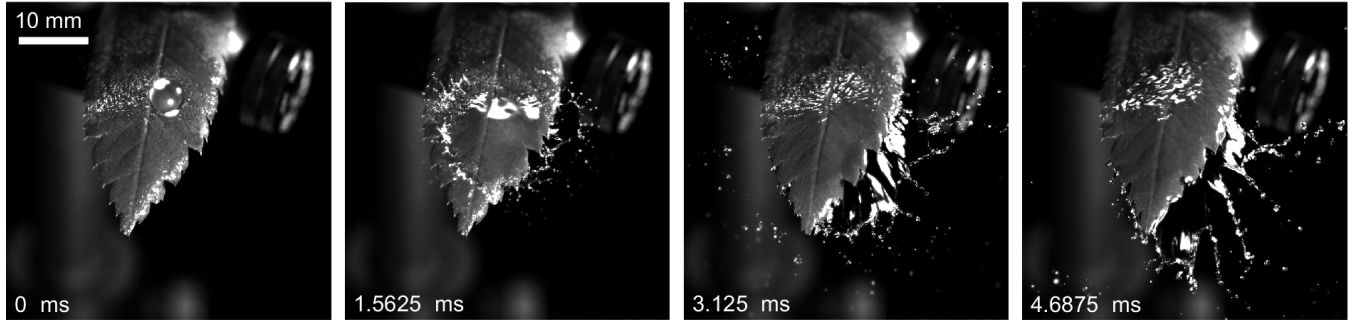

FIG. 1. Time sequence of the impact of a drop on a leaf of *Sorbus aucuparia*, commonly known as rowan. There are many teeth at the edge of the leaf blade. The time of impact is in 0 ms. At 1.5625 ms, water reaches the leaf edge. At 3.125 ms, a non-circular liquid sheet surrounded by a rim is formed beyond the leaf edge. At 4.6875 ms, the sheet and rim have started fragmenting in droplets that are ejected in preferential directions. The maximum width of the leaf blade is approximately 19 mm. The corresponding movie is available in the supplemental material.

Both raindrops and drips have a significant chance of impacting at less than about a centimeter from the edge of a plant leaf. In such case, the impacting drop spreads beyond this edge and forms a liquid sheet surrounded by a rim from which droplets are ejected [11, 12]. Similar droplet ejections occur when raindrops impact near or onto other sessile drops or puddles left on the leaves from previous impacts [9, 12, 13]. As the impacting drop dissipates its kinetic energy upon spreading on the leaf surface, the earlier it reaches the edge, the more momentum it may transfer to the rim and ejected droplets [11]. Nevertheless, leaf edges are often irregular, with lobes or teeth (Fig. 1), so the distance travelled by the fluid from the impact point to the edge depends on which direction is considered. Consequently, the edge shape should influence the rim dynamics and the resulting ejection pattern. This is already suggested by

---

the snapshots of Figure 1 that shows a drop impact on a leaf of *Sorbus aucuparia*. The teeth of this leaf are a few millimeters long. It is observed that the rim and subsequent droplets go farther in the directions corresponding to troughs in the leaf edge profile. The present paper aims at unveiling this signature of the edge shape. Many other parameters are known to influence the dynamics of such drop impacts, including substrate roughness [14], compliance [9] and inclination [12]. These other parameters are highly variable in plant leaves. Nevertheless, as this paper will show, the edge-induced shaping of rim and ejections observed with a plant leaf (Fig. 1) is qualitatively similar to that observed with smooth, rigid and horizontal star-shaped poles with teeth of similar dimensions (Fig. 2). For the sake of simplicity and in a reductionist approach, this paper focuses on the latter configuration and leaves the potential influence of roughness, compliance and inclination to future work.

Most studies on droplet ejection from the rim of a sheet focused on axisymmetric configurations, e.g., a drop impacting the center of the flat, top face of a pole [15]. The main relevant parameters are the drop diameter D, its impact speed U, the ratio S_a between the pole diameter and the drop diameter, and the water properties (density ρ, viscosity μ and surface tension σ). The sheet first expands as the rim moves outward beyond the edge. The rim decelerates in response to the pulling from the sheet (surface tension forces), and it destabilises into ligaments from which droplets are emitted. The sheet finally shrinks as the rim moves back inward [15]. The collision of rim segments emits even more droplets, sometimes through the formation of secondary sheets called fines [16]. The sheet and rim dynamics are mainly characterized through the radial position of the rim R_a vs. time t. It was rationalized with models of increasing complexity, from a harmonic oscillator [15] or a third-degree polynomial [17] to a full description of mass and momentum balance between sheet, rim and droplets [18]. All the models converge on one key point: the time at which the sheet reaches its maximal extension scales as the capillary time $t_\sigma = \sqrt{\rho D^3/(6\sigma)}$. The Weber number $\mathrm{We} = \rho D U^2/\sigma$ represents the ratio of kinetic and surface energy of the initial drop. Its square root corresponds to the ratio between the capillary time and the impact time $t_i = D/U$, which is the timescale needed for the drop to crush on the pole. A complete transfer of the drop kinetic energy into surface energy of the sheet would yield a maximum sheet radius equal to $D/2\sqrt{\mathrm{We}/12}$. This scaling law is well-verified experimentally, although with an additional factor, less than unity, that takes into account energy dissipation at the pole surface (boundary layer) and in the rim [17]. The Ohnesorge number $\mathrm{Oh} = \mu/\sqrt{\rho \sigma D}$ represents the influence of viscosity at the sheet timescale t_σ. In the considered impacts that lead to sheet formation, $\mathrm{We} \gg 100$ and $\mathrm{Oh} \ll 1$, so the sheet is much larger than the initial drop and its expansion is moderately influenced by viscosity. Several works investigated extensions of this configuration to viscoelastic liquids (e.g., [19]) or very small poles with $S_a < 1$ [20].

As the rim decelerates, its thickness increases in order to maintain a balance between inertial and capillary forces [21]. The rim systematically experiences an azimuthal instability in which it becomes corrugated. This has been explained through a combination of Rayleigh-Taylor and Rayleigh-Plateau instabilities [22]. The rim corrugations grow to the point where they form ligaments [23]. Droplets are mainly ejected from the tip of these ligaments. Nevertheless, smaller, satellite droplets may also be ejected during ligament pinch-off, and larger droplets may be ejected when two ligaments merge [24]. The droplet size is inherited from the ligament width [24]. Its distribution can be approximated, among others, by a Gamma function [17]. The droplet speed is inherited from the rim speed and it consequently decreases with increasing time of ejection [24]. The number of ligaments N_ℓ increases proportionally to $\mathrm{We}^{3/8}$ and slightly decreases with time [23]. At $\mathrm{We} \simeq 950$, $\mathrm{Oh} = 1.8 \times 10^{-3}$ and $S_a = 1.45$, $N_\ell \simeq 35$ [23]. Azimuthal variations of sheet thickness were observed for similar impact parameter values [25], although the number of periods was about 24, i.e., not coincident with N_ℓ. Similar azimuthal instabilities were observed in other drop impact configurations, e.g., on thin films [26, 27] and in crown splash [28].

The ingredient "edge shape" can be introduced into this axisymmetric configuration by considering non-circular substrate shapes, with a symmetry of order N. Juarez *et al.* [29] investigated drop impacts at the center of substrates shaped as regular convex polygons with $N \in [3, 10]$ sides. The cross-sectional area of the polygons was kept constant and equal to $\pi D^2/4$, which corresponds to an angle-averaged distance to the edge $S_a \simeq 1$ (once normalized by drop radius). The study focused on drops of water-glycerol solutions impacting at relatively low speed ($\mathrm{We} < 200$, $\mathrm{Oh} > 0.01$). This regime does not correspond to raindrops of any size at terminal speed. The spreading drop reaches the polygon edges first in the directions normal to these edges, and last in the directions of the polygon vertices. Consequently, the rim inherits more kinetic energy and goes farther in the former directions than in the latter. The amplitude of this azimuthal asymmetry grows with time. At maximum extension, the rim looks alike the polygonal pole rotated by π/N. The directions of maximal rim extension are also those where droplets are preferentially ejected. Since regular convex polygons approach a circle as N is increased, the polygonal shape cannot be recognized anymore when $N > 7$ [29]. Indeed, the azimuthal variations of rim radius induced by the polygon become negligible with respect to the intrinsic rim corrugations discussed earlier for circular poles. As a side note, polygonal spreading and break-up was also observed with drops bouncing on superhydrophobic star-shaped ridges [30], drops impacting superhydrophobic surfaces covered with a regular lattice of micropillars [14, 31], or jets impacting such surfaces [32]. In all these cases, the mechanism is the same: the fluid travels farther in directions that were unobstructed by the substrate topography.

In this paper, we explore the dynamics of drop impacts on star-shaped substrates, in a regime experienced by raindrops and drips. We aim at quantifying the modifications induced by the substrate shape on the motion of the rim formed once the fluid spreads beyond the substrate edge, and on the subsequent droplet ejections. Section II comprises the materials and methods. In section III, several key experimental observations are described. In section IV (resp. section V), quantitative results on the sheet and rim kinematics (resp. the ejected droplets) are presented and discussed. Section VI is the conclusion.

II. MATERIALS AND METHODS

A. Experimental setup

Drops of water (density $\rho \simeq 1000$ kg/m^3, viscosity $\mu \simeq 1$ mPa.s, surface tension $\sigma \simeq 0.07$ N/m) were released from a nozzle. This nozzle was a male Luer-lock that generated drops of diameter $D \simeq 4.95$ mm (volume $\simeq 63$ μL). The corresponding Ohnesorge number is Oh = 0.0017. The flow in the nozzle was regulated thanks to a syringe pump (World Precision Instruments, AL-300) operated manually to record one impact at a time (drips were separated by several seconds). Ten different impact speeds of the drops were experimented by changing their fall height, i.e., the height of the nozzle relative to the impact point (Table I). The corresponding Weber number varied in the range $[835, 1872]$, which is significantly higher than the regime explored in [29]. In the remainder of this work, times are normalized by the capillary time $t_\sigma = \sqrt{\rho D^3/(6\sigma)} = 16.7$ ms, and lengths are normalized by the radius of the impacting drop $D/2 = 2.475$ mm.

TABLE I. Ten fall heights H of the impacting drop, corresponding impact speed U and Weber number We, and associated symbol in subsequent graphs.

H [m]	U [m/s]	We	Symbol
0.725	3.51	835	▲
0.825	3.74	950	▼
0.925	3.96	1065	◄
1.025	4.17	1180	►
1.125	4.37	1296	●
1.225	4.56	1411	■
1.325	4.74	1526	✳
1.425	4.92	1641	∗
1.525	5.09	1756	◆
1.625	5.25	1872	★

The considered substrate was a horizontal aluminum disk with $N = 10$ triangular teeth on the outer edge. It was fabricated by wire electric discharge machining (accuracy of the order of 5 μm) and polished afterwards. The resulting arithmetic average roughness was $0.4(\pm 0.1)$ μm (average and standard deviation of measurements on three substrates in four different directions). The substrate was mounted on a metal rod of diameter 6 mm fixed vertically on a stage that could be translated horizontally in order to position the substrate exactly below the nozzle.

The radial position of the substrate edge is denoted $S(\theta)$, where θ is the polar angle in the horizontal plane, measured from a trough of the teeth profile. The radial position of the troughs (resp. peaks) is S_t (resp. S_p). In all the considered substrates, this trough radius $S_t \simeq 2.52$ (i.e., 6.25 mm), while the peak radius S_p varied between 2.92 and 4.54 (i.e., between 1 mm and 5 mm from troughs to peaks). This teeth size is comparable to that observed in the plant leaf of Fig. 1. The edge shape satisfies

$$S = \frac{S_t S_p \sin\left(\frac{\pi}{N}\right)}{S_t |\sin\varphi| + S_p \left[\sin\left(\frac{\pi}{N}\right)\cos\varphi - \cos\left(\frac{\pi}{N}\right)|\sin\varphi|\right]}, \tag{1}$$

where $\varphi \in [-\pi/N, \pi/N]$ is an angle defined by

$$\varphi + \frac{\pi}{N} = \left[\theta + \frac{\pi}{N}\right]\left(\mathrm{mod}\frac{2\pi}{N}\right). \tag{2}$$

The edge function $S(\theta)$ is even and can be decomposed in a cosine Fourier series,

$$S(\theta) = S_a + \sum_{j=1}^{\infty} \alpha_j \cos(j\theta), \tag{3}$$

where

$$S_{\mathrm{a}} = \frac{1}{2\pi} \int_0^{2\pi} S(\theta) \mathrm{d}\theta, \text{ and } \alpha_j = \frac{1}{\pi} \int_0^{2\pi} S(\theta) \cos(j\theta) \mathrm{d}\theta. \tag{4}$$

By rotational symmetry, $\alpha_j = 0$ when $j/N \notin \mathbb{N}_0$. The first four Fourier coefficients corresponding to the 6 considered substrates are given in table II.

TABLE II. First four Fourier coefficients of the substrate shape $S(\theta)$, for $S_{\mathrm{t}} = 2.52$ and the 6 considered values of S_{p}. All these lengths have been normalized by $D/2$. The last column indicates the color of symbols corresponding to each substrate in subsequent graphs.

Substrate #	S_{p}	S_{a}	α_{10}	α_{20}/α_{10}	α_{30}/α_{10}	Color
1	2.92	2.69	-0.16	-0.12	0.12	◀
2	3.33	2.87	-0.32	-0.06	0.06	◀
3	3.74	3.03	-0.48	-0.04	0.04	◀
4	3.86	3.07	-0.52	-0.04	0.04	◀
5	4.14	3.17	-0.63	-0.03	0.03	◀
6	4.54	3.31	-0.78	-0.02	0.02	◀

The drop impacts were imaged with a high-speed camera (Photron Fastcam Mini UX100) and a macro lens (Zeiss Milvus 2/100M). Videos were recorded at 6400 frames per second with a resolution of 80 μm/pix. The camera was mounted above the substrate, providing a top-view with an inclination of $\leq 5°$. The exposure time was always less than 10 μs. Consequently, strong back lighting was required to observe the sheet, rim and droplet dynamics with sufficient contrast. A light-diffusing sheet was installed between the light source and the substrate to provide a clear and sufficiently homogeneous background.

The trajectory of free-falling drops is not a straight vertical line [33]. Consequently, even if the nozzle was not moved horizontally, the impact point was scattered over an area increasing with fall height H and reaching a maximum of almost 1 cm^2 in the present experiments. Although the impact point could not be directly seen because the substrate was opaque and back-lit, off-centered impacts generated strongly asymmetric liquid sheets. Only 17 impacts yielding sheets that were almost perfectly centered were considered for data processing. The impact speed (i.e., the Weber number) and the teeth length were systematically varied (cf. tables I and II). Three replicas of the experiment at We = 1065 with substrate 4 are reported to assess reproducibility. The influence of viscosity (considering a water-glycerol solution) and off-centering is qualitatively described in section III but these variations are not considered in the quantitative analysis.

B. Data processing

In each video, the substrate edge, the liquid sheet, and the ejected droplets were segmented thanks to elementary image processing. We checked with side view movies that the sheet and droplets remain in the horizontal plane of the substrate. This happens because the substrate is sufficiently large to fully deflect the impacting drop ($S_{\mathrm{a}} > 1.5$), as already observed in [11]. Moreover, gravity has no time to significantly bend the sheet downward during its expansion. This is in sharp contrast with the substrates at $S_{\mathrm{a}} \simeq 1$ studied in [29], for which the sheet was then always strongly inclined. In our experiments, the sheet could only be tracked properly once the rim was fully detached from the substrate. Its tracking also failed at some point during retraction. These two limits defined the time range in which the positions of the sheet edge (i.e., the inner side of the rim) and the droplets were recorded. The radial position of both the substrate edge $S(\theta)$ and the sheet edge $R(\theta, t)$ were recorded at each time (Fig. 2). Droplets were only kept if they were detected on at least five different frames, at a position that corresponded to a trajectory at constant velocity. For each droplet, the time of ejection t_{d} (i.e., the first time at which the droplet was detected), the corresponding angular position θ_{d}, the droplet speed v_{d} and its direction θ_{v} (relative to θ_{d}) were recorded (Fig. 2). All the variables and their meaning are listed in table III.

The sheet edge profile is also decomposed in a Fourier series that now includes both cosine and sine terms in θ:

$$R(\theta, t) = R_{\mathrm{a}}(t) + \sum_{j=1}^{\infty} A_j(t) \cos(j\theta) + \sum_{j=1}^{\infty} B_j(t) \sin(j\theta), \tag{5}$$

with

$$R_{\mathrm{a}}(t) = \frac{1}{2\pi} \int_0^{2\pi} R(\theta, t) \mathrm{d}\theta, \quad A_j(t) = \frac{1}{\pi} \int_0^{2\pi} R(\theta, t) \cos(j\theta) \mathrm{d}\theta, \quad B_j(t) = \frac{1}{\pi} \int_0^{2\pi} R(\theta, t) \sin(j\theta) \mathrm{d}\theta. \tag{6}$$
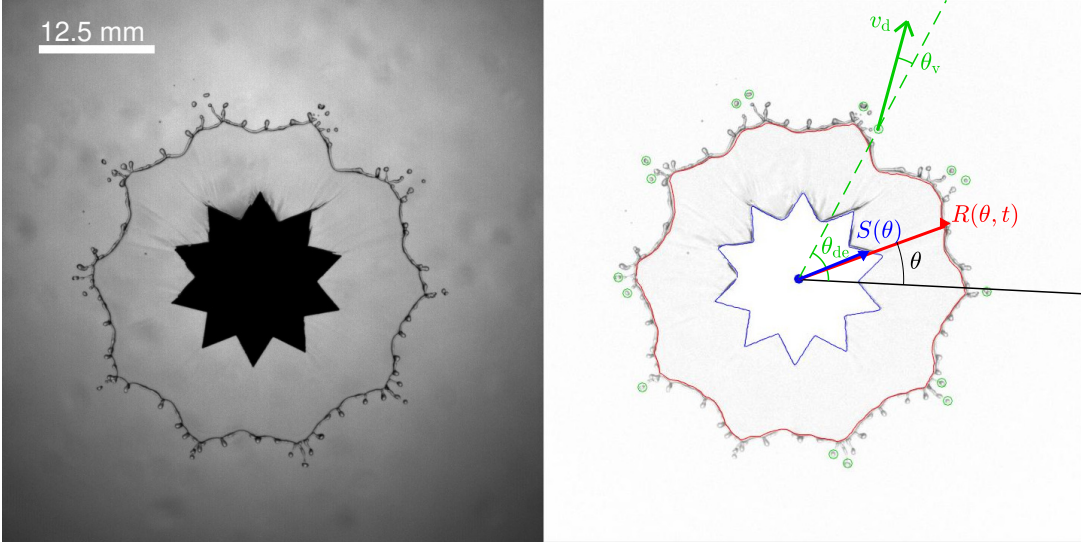
FIG. 2. (Color online) Image processing: the left picture is a snapshot from the raw video. In this picture, the substrate diameter (from peak to peak) is $2S_p = 7.72$ (namely, 19.1 mm). The right picture shows items tracked by image processing on that snapshot: the substrate edge (blue) at radial position $S(\theta)$, the sheet edge (red) at radial position $R(\theta, t)$, and the droplets (green) at angular position θ_d. The droplets were ejected at speed v_d in direction θ_v (relative to θ_d).

Although the impact point was not visible on the videos, its position could be inferred from the first harmonics of $R(\theta, t)$, i.e., $j = 1$ in the sums of equation (5), at the earliest time where the sheet could be detected. All the processed impacts were taken at a distance $\sqrt{A_1^2 + B_1^2} < 1.5$ mm from the symmetry center of the substrate.

In order to evaluate the extent to which the substrate edge shapes the rim and sheet, we focus on the harmonic of coefficient $A_N(t)$. The residue χ is defined as the standard deviation of the remainder, namely

$$\chi(t) = \sqrt{\frac{1}{2\pi} \int_0^{2\pi} \left[R(\theta, t) - R_a(t) - A_N \cos(N\theta) - A_1 \cos\theta - B_1 \sin\theta \right]^2 d\theta} = \frac{1}{\sqrt{2}} \sqrt{\sum_{j=2}^{N} (A_j^2 + B_j^2) - A_N^2}. \quad (7)$$

In this definition of the residue, the modes of coefficients A_1 and B_1 are also removed, as they mostly result from the offset of the impact point.

III.   PHENOMENOLOGY

Figure 3 illustrates the time evolution of the liquid rim from the moment where it reaches the peaks of the substrate edge. At that time, the rim is still approximately circular. As it moves radially outward, it is progressively shaped in a way reminiscent of the substrate edge (time 1.5625 ms in Fig.3): it goes farther in the directions corresponding to edge troughs and less far in directions corresponding to edge peaks, similarly to what was observed for polygonal substrates [29]. As the rim decelerates, it becomes corrugated and it is destabilized. At time 3.125 ms in Fig. 3, ligaments are formed [23]. They subsequently break-up into droplets that are ejected outward as they largely inherit the speed of the rim [24]. Impacts at two different Weber numbers are compared in Fig. 3. Both yield rims that are visibly shaped by the substrate geometry. At equivalent times, the rim goes farther at higher We, and the ejected droplets are smaller [17].

Figure 4 shows a snapshot sequence of the impact of a drop made of a water-glycerol solution (mixing ratio 10:13). The corresponding viscosity is $\mu \simeq 10$ cP, i.e., 10 times higher than in other experiments (with plain water). The corresponding Ohnesorge number is Oh $= 0.017$. This increase of viscosity certainly translates into an increased viscous dissipation in the boundary layer formed as the drop spreads on the substrate [34]. Consequently, the angle-averaged maximum extension of the sheet and rim is decreased. Rim variations induced by the substrate geometry appear more pronounced, especially since the rim is observed to remain pinned at the tip of the substrate teeth (cf. second and third snapshots of Fig. 4). Ligaments only grow in the direction of edge troughs, resulting in highly defined directions of droplet ejection (snapshot 4 of Fig. 4).

Figure 5 shows the spreading of a drop that impacted a few millimeters from the center of substrate 5. In such case, the radial growth of the rim is strongly asymmetric, showing a much larger extension in the direction corresponding to the shortest path from impact point to substrate edge. In the opposite direction, the rim barely surpasses the edge teeth, owing to the large travel distance on the substrate and subsequent dissipation. The rim tips, where large ligaments develop, are still aligned with the troughs of the substrate edge but their orientation is not radial anymore.

IV. SHEET AND RIM KINEMATICS

The time evolution of the angular average of the sheet edge $R_a(t)$ is shown in Figure 6 for all processed experiments. The sheet expands outward, decelerates, and then retracts inward. The axisymmetric evolution of the rim resulting from centered impacts on circular poles has been observed and explained in several papers with models of variable complexity [15, 17, 18, 25]. The angle-averaged component of $R(\theta, t)$ (namely $R_a(t)$) would also likely be captured by these axisymmetric models. Nevertheless, we take a different approach [11, 12]. We check that, empirically, the increasing part of $R_a(t)$ (expanding sheet) is very-well approximated by a second-degree polynomial in t through linear least-square fitting. The time t_{ae} at which the average sheet edge R_a would reach the average substrate edge S_a is determined from this polynomial, which can then be rewritten as

$$R_a(t) \simeq S_a + \dot{R}_{ae}(t - t_{ae}) + \ddot{R}_{ae}\frac{(t - t_{ae})^2}{2},$$ (8)

where the initial rim speed $\dot{R}_{ae} = \dot{R}_a(t_{ae})$ and constant acceleration $\ddot{R}_{ae} = \ddot{R}_a(t_{ae})$ correspond to the two other degrees of freedom of the fit. The time $\tau = t - t_{ae}$ is defined as the average time of the rim off the substrate. The second-degree polynomial approximating $R_a(t)$ can be rewritten:

$$R_a(\tau) \simeq S_a + \dot{R}_{ae}G(\tau), \qquad G(\tau) = \tau\left(1 - \frac{\tau}{2\tau_M}\right), \qquad \tau_M = -\frac{\dot{R}_{ae}}{\ddot{R}_{ae}}.$$ (9)

The function $G(\tau)$ contains the description of the sheet and rim dynamics, and although it was empirically chosen as a second-degree polynomial, any more complex and realistic model of this dynamics could be incorporated in $G(\tau)$.

TABLE III. List of main variables

| Variable	Definition	Expressed as normalized by
θ	Polar angle	-
φ	Polar angle, modulo $2\pi/N$	-
θ_v	Direction of droplet ejection, relative to the position of ejection	-
t	Time from impact	t_σ
τ	$t - t_{ae}$	t_σ
We	Weber number	-
N	Number of teeth of the substrate	-
$S(\theta)$	Radial position of substrate edge	$D/2$
S_p	Substrate radius at peaks	$D/2$
S_t	Substrate radius at troughs	$D/2$
$R(t, \theta)$	Radial position of the sheet edge (i.e., the inner side of the rim)	$D/2$
$R_s(t)$	Radial position of the rim on the substrate	$D/2$
α_j	j-th coefficient of the Fourier series of $S(\theta)$	$D/2$
A_j	j-th cosine coefficient in the Fourier series of $R(t, \theta)$	$D/2$
B_j	j-th sine coefficient in the Fourier series of $R(t, \theta)$	$D/2$
χ	Residue of the Fourier series	$D/2$
R_{sM},	Maximum radius of the rim on an unbounded substrate	$D/2$
t_{sM}	Time at which R_{sM} is reached	t_σ
T	t/t_{sM}	-
v_d	Speed of ejected droplets	U
Ω_d	Volume of ejected droplets	$\pi D^3/6$
Used indices for a variable X		
X_a	Average of $X(\theta)$ along θ	
$X_e(\theta)$	When the rim reaches the edge of the substrate at angular position θ.	
X_{ae}	When the angle-averaged rim reaches the edge of the substrate.	
X_d	Relative to the droplets at the time of their ejection	
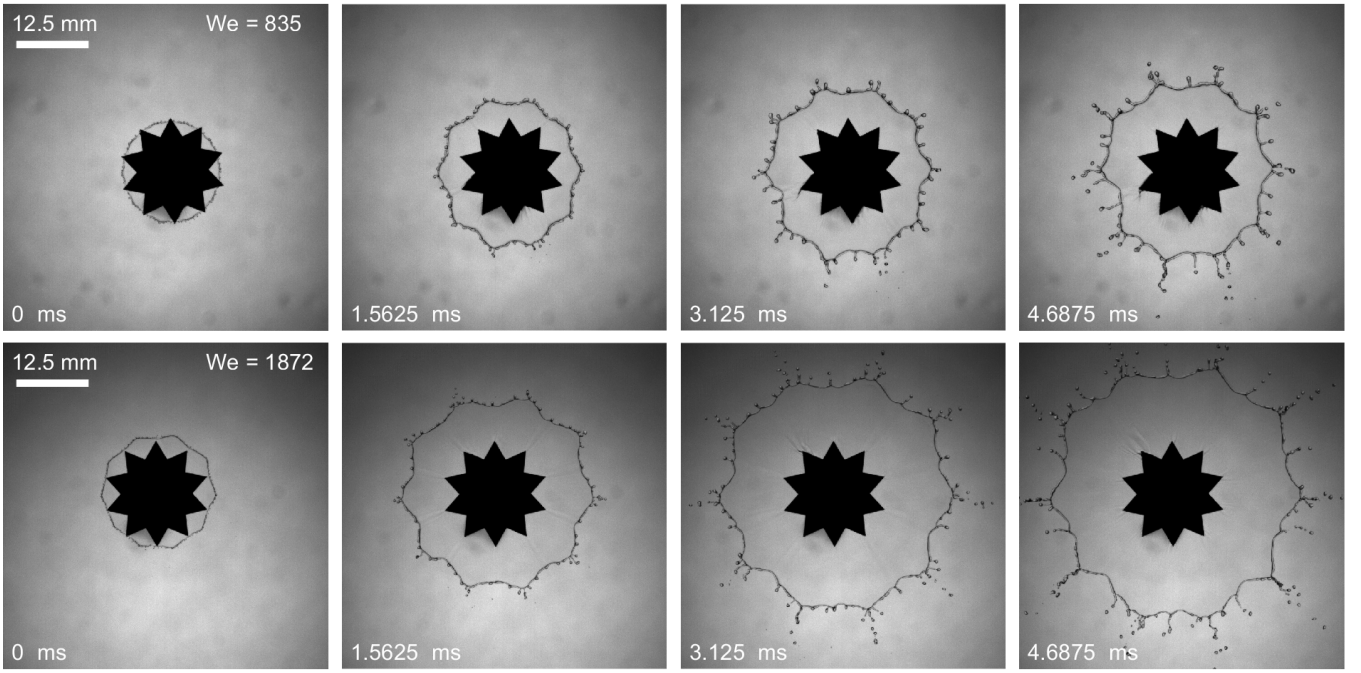
FIG. 3. Snapshots showing the evolution with time of two drop impacts on substrate 4, at We = 835 (top row) and We = 1872 (bottom row), respectively. The time is measured from the moment the rim crosses the peaks of the substrate edge. The substrate diameter (from peak to peak) is $2S_\mathrm{p}$ = 7.72 mm. The corresponding movies are available in the supplemental material.
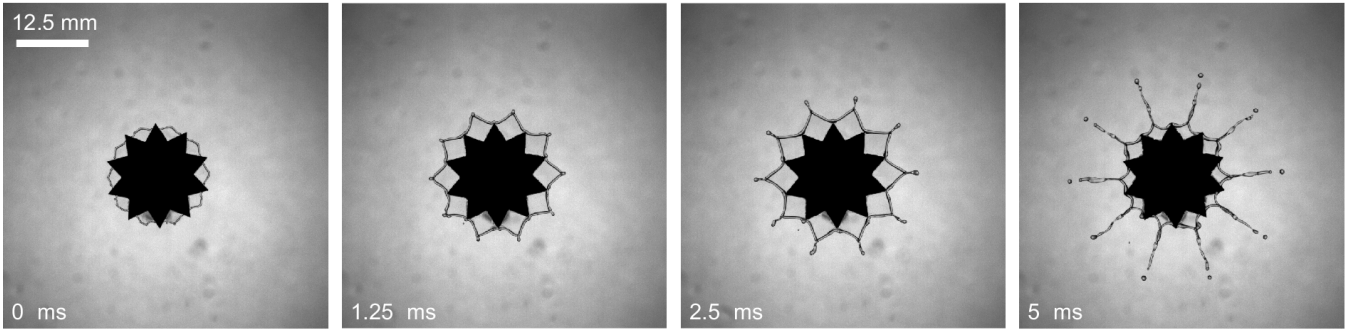

FIG. 4. Snapshots showing the evolution with time of a drop impact on substrate 4, at We = 1411 (top row). The time is measured from the moment the rim crosses the peaks of the substrate edge. The substrate diameter (from peak to peak) is $2S_\mathrm{p}$ = 7.72 mm. By contrast with the other snapshots, the drop is here made of a water-glycerol mixture of viscosity μ = 10 cP. Pinning of the rim at the teeth peaks is observed. The corresponding movie is available in the supplemental material.

The measured angle-averaged initial rim speed $\dot{R}_\mathrm{ae}$ should somehow be inherited from the dynamics of earlier spreading on the substrate. Again, several models capture this dynamics, each in a specific range of impact and substrate parameters [35–39]. Therefore, we keep the formulation as general as possible. On a horizontal and unbounded solid, the rim radius $R_\mathrm{s}(t)$ obeys

$$R_\mathrm{s}(t) = R_\mathrm{sM}F(T), \tag{10}$$

where R_sM is the maximum spreading radius on the solid, $T = t/t_\mathrm{sM}$ is a normalized time, t_{sM} is the time at which this radius would be reached, and $F(T)$ is a function to be determined. This function must satisfy $F' > 0$ and $F'' < 0$ for $T \in [0, 1[$ and $F' = 0$ in $T = 1$. Measurements of the spreading dynamics on a large aluminum plate (i.e., where the spreading drop does not reach the plate edges) are provided in appendix A, together with an empirical expression
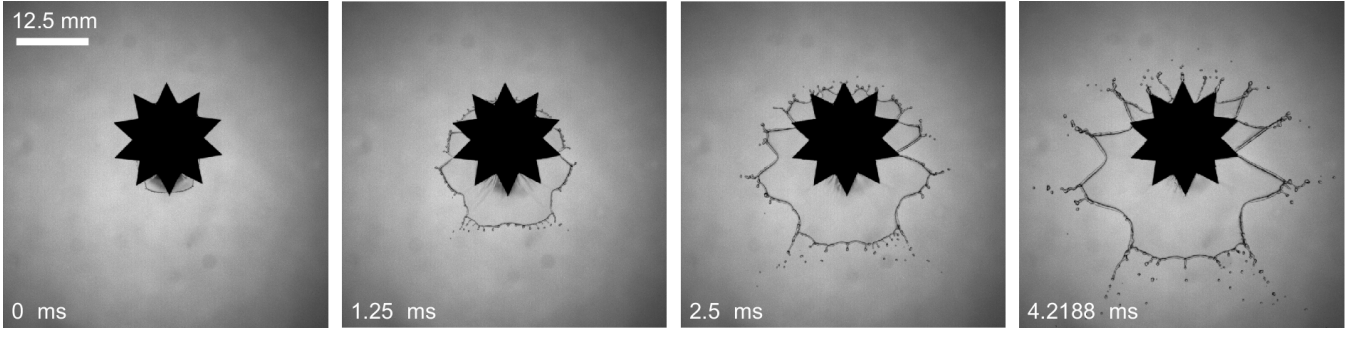
FIG. 5. Snapshots showing the evolution with time of a strongly off-centered drop impact on substrate 5, at We = 1065. The time is measured from the moment the rim crosses the peaks of the substrate edge. The substrate diameter (from peak to peak) is $2S_\mathrm{p} = 8.28$ mm. The corresponding movie is available in the supplemental material.
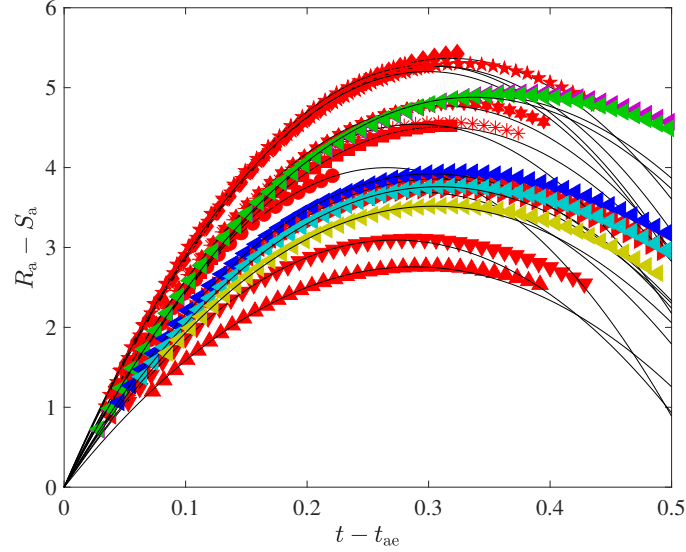

FIG. 6. (Color online) Angle-averaged distance between sheet and substrate edges, $R_\mathrm{a}(t) - S_\mathrm{a}$, as a function of time t (shifted by the time t_ae at which $R_\mathrm{a} = S_\mathrm{a}$). The black solid lines correspond to the second-degree polynomial approximations of equation (8). Symbols (resp. colors) correspond to different We (resp. α_N), as described in table I (resp. II).

for $F(T)$ and scaling laws for R_sM and t_sM vs. We and Oh. According to equation (10), the time t_ae at which the rim reaches the substrate edge is the solution of

$$S_\mathrm{a} = R_\mathrm{sM} F(T_\mathrm{ae}), \qquad T_\mathrm{ae} = t_\mathrm{ae}/t_\mathrm{sM}. \tag{11}$$

The corresponding rim speed would then be

$$\dot{R}_\mathrm{s}(t_\mathrm{ae}) = \frac{R_\mathrm{sM}}{t_\mathrm{sM}} F'(T_\mathrm{ae}). \tag{12}$$

The rim speed on the substrate $\dot{R}_\mathrm{s}(t_\mathrm{ae})$ is predicted from the expressions of R_sM and t_sM determined in appendix A. Then, in figure 7, it is compared to the rim speed once off the substrate as extrapolated from measurements of $R_\mathrm{a}(t)$. In good approximation,

$$\dot{R}_\mathrm{ae} \simeq 0.88 \dot{R}_\mathrm{s}(t_\mathrm{ae}), \tag{13}$$

which confirms that the initial speed of sheet expansion is largely inherited from the rim speed on the substrate.

The normalized time at which the sheet reaches a maximum of average extension R_a is measured as $\tau_\mathrm{M} \simeq 0.30 \pm 0.02$ (mean $\pm$ standard deviation over all experiments) so it may be considered as constant in the present experimental
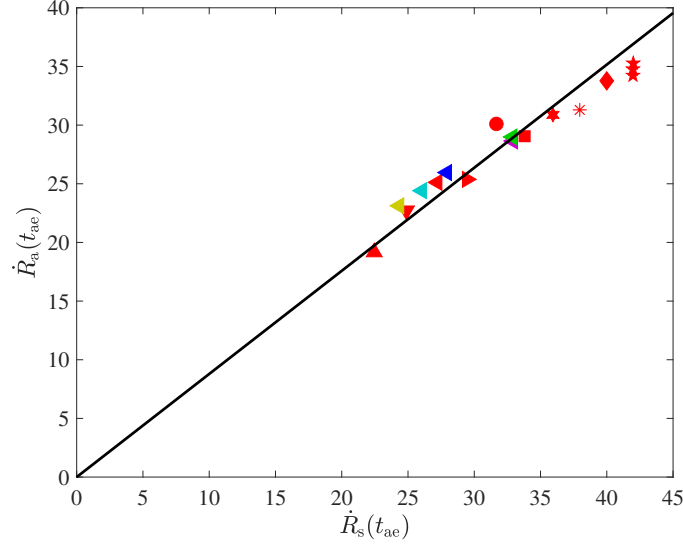
FIG. 7. (Color online) Initial radial speed of the sheet edge $\dot{R}_{ae}$, obtained by extrapolation of its radial position to $R_a(t_{ae}) = S_a$, vs. speed $\dot{R}_s(t_{ae})$ of the rim on an unbounded substrate predicted by equation (12). The solid line corresponds to equation (13). Symbols (resp. colors) correspond to different We (resp. α_N), as described in table I (resp. II).

dataset. Nevertheless, this time increases slightly with We (coefficient of correlation 0.5, coefficient of determination 0.25 for a linear fit) and decreases with increasing S_m (coefficient of correlation -0.9, coefficient of determination 0.82 for a linear fit). The latter dependence was already noted for drop impacts next to a straight substrate edge [12].
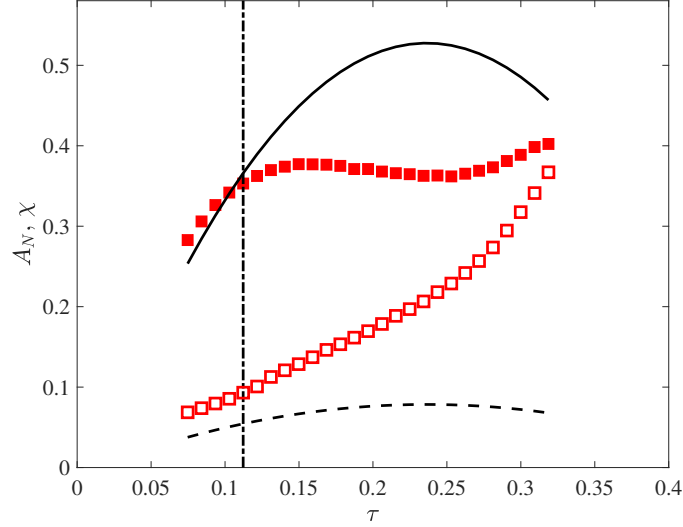

FIG. 8. Evolution of the component A_N mainly excited by the substrate edge shape (thick full symbols) and the residue χ (thick empty symbols) with time τ. The solid (resp. dashed) line corresponds to the prediction of equation (21) for A_N (resp. χ). The dash-dotted line indicates the time at which the first droplets are ejected from the rim. In this experiment, We = 1411 and $\alpha_N = -0.52$.

An example of time evolution of the sheet edge coefficient A_N and the residue χ is shown in figure 8. In all experiments, the coefficient A_N remained significantly larger than the residue χ as long as the sheet expanded ($\tau < 0.3$). It confirms that the shape of the expanding sheet is mostly influenced by the substrate shape. The growth of coefficient A_N always ends earlier than the average sheet expansion. In figure 8, A_N reaches a maximum around 0.4 in $\tau \simeq \tau_M/2$. This maximum is comparable to $-\alpha_N$, which suggests that the angular variations of the sheet radius are of the same order as those of the substrate edge. In every experiment, χ increased monotonously with time and became comparable to A_N by the time the sheet reached its maximum extension.

The variation of A_N at early times may be rationalized as follows. We first hypothesize that equation (9), describing the evolution of the angle-averaged sheet radius $R_{\mathrm{a}}(\tau)$, can be generalized to predict the sheet radius at any angle $R(\tau, \theta)$:

$$R(\tau, \theta) = S(\theta) + 0.88\dot{R}_{\mathrm{s}}(t_{\mathrm{e}})G(\tau - \tau_{\mathrm{e}}), \quad \tau_{\mathrm{e}}(\theta) = t_{\mathrm{e}}(\theta) - t_{\mathrm{ae}}, \tag{14}$$

where $t_{\mathrm{e}}(\theta)$ is the time at which the rim reaches the substrate edge in direction θ. This time can be obtained by solving

$$R_{\mathrm{sM}}F[T_{\mathrm{e}}(\theta)] = S(\theta) \tag{15}$$

with $T_{\mathrm{e}}(\theta) = t_{\mathrm{e}}(\theta)/t_{\mathrm{sM}}$. Assuming that the substrate edge is only slightly corrugated (i.e., $|S(\theta) - S_{\mathrm{a}}| \ll S_{\mathrm{a}}$), T_{e} can be estimated through a Taylor approximation of equation (15),

$$T_{\mathrm{e}}(\theta) = T_{\mathrm{ae}} + \frac{S(\theta)/R_{\mathrm{sM}} - F_{\mathrm{ae}}}{F'_{\mathrm{ae}}}, \tag{16}$$

where $F_{\mathrm{ae}} = F(T_{\mathrm{ae}})$ and $F'_{\mathrm{ae}} = F'(T_{\mathrm{ae}})$. With a second Taylor approximation now on $F'(T_{\mathrm{ae}})$, we estimate the rim speed once it locally reaches the substrate edge:

$$\dot{R}_{\mathrm{s}}(t_{\mathrm{e}}) = \frac{R_{\mathrm{sM}}}{t_{\mathrm{sM}}}F'(T_{\mathrm{e}}) \simeq \frac{R_{\mathrm{sM}}}{t_{\mathrm{sM}}}\left[F'_{\mathrm{ae}} + F''_{\mathrm{ae}}(T_{\mathrm{e}}(\theta) - T_{\mathrm{ae}})\right], \qquad F''_{\mathrm{ae}} = F''(T_{\mathrm{ae}}). \tag{17}$$

Finally, a Taylor approximation of the angular dependence of $G(\tau)$ is considered:

$$G(\tau - \tau_{\mathrm{e}}) = G(\tau) - G'(\tau)\tau_{\mathrm{e}}. \tag{18}$$

Consequently,

$$R(\tau, \theta) \simeq S(\theta) + 0.88\frac{R_{\mathrm{sM}}}{t_{\mathrm{sM}}}\left[F'_{\mathrm{ae}} + F''_{\mathrm{ae}}(T_{\mathrm{e}} - T_{\mathrm{ae}})\right]\left[G(\tau) - G'(\tau)\tau_{\mathrm{e}}\right]. \tag{19}$$

Under the same hypothesis of a slightly corrugated substrate, $|T_{\mathrm{e}} - T_{\mathrm{ae}}| \ll T_{\mathrm{ae}}$ and

$$R(\tau, \theta) \simeq S(\theta) + 0.88\frac{R_{\mathrm{sM}}}{t_{\mathrm{sM}}}F'_{\mathrm{ae}}G(\tau) + 0.88\left[S(\theta) - S_{\mathrm{a}}\right]\left[\frac{F''_{\mathrm{ae}}}{F'_{\mathrm{ae}}t_{\mathrm{sM}}}G(\tau) - G'(\tau)\right]. \tag{20}$$

Equation (9) is recovered by averaging this equation along θ. The other Fourier coefficients of $R(\tau, \theta)$ are given by:

$$\begin{cases} A_j(\tau) = \alpha_j\left[1 + 0.88\left(\frac{F''_{\mathrm{ae}}}{F'_{\mathrm{ae}}t_{\mathrm{sM}}}G(\tau) - G'(\tau)\right)\right] \\ B_j(\tau) = 0 \end{cases} \tag{21}$$

The prediction made by equation (21) for $A_N(\tau)$ is shown in figure 8. At the first instants of the sheet expansion, the prediction looks very good, especially since there is no additional fitting parameter once $R_{\mathrm{a}}(\tau)$ is prescribed.

In figure 8, the model prediction fails at $\tau \gtrsim 0.11$. Although this time limit varies from one experiment to another, it always remains close to the time at which the first droplets are ejected from the rim. We indeed expect that the dynamical behavior of the rim changes once it starts losing mass through droplet ejections.

According to equation (21), all the modes j would obey to the same time evolution, and so would do the residue χ. This is disproved by figure 8 in which χ is not proportional to A_N. Moreover, equation (21) systematically underestimates $\chi(t)$. This disagreement certainly originates from the two strong hypotheses inherent to this model: the fact that the rim and sheet would evolve independently in each direction as specified by equation (14), and the fact that the substrate would be slightly corrugated (cf. Taylor approximations).

The aforementioned shortcomings suggest that the model should only be appropriate to rationalize the initial growth of $A_N(\tau)$. The parity plot of figure 9 compares the prediction of equation (21) to measurements taken at most 0.042 (i.e., 0.7 ms) after the rim fully detached from the substrate edge. The agreement is remarkably good (coefficient of determination 0.92), again considering that there is no fitting parameter once the angle-averaged rim evolution is given. In particular, the coefficient A_N is always positive at the considered times (Figs. 8 and 9), while $\alpha_N < 0$ (Table II), which corroborates the fact that the rim expands faster in directions corresponding to edge troughs.
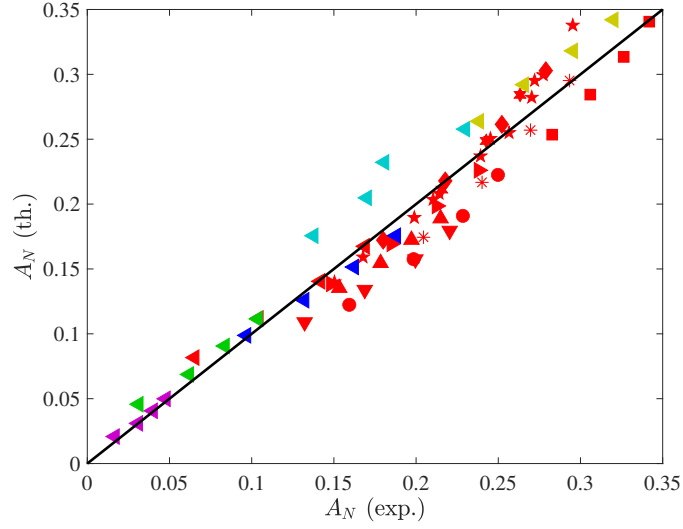
FIG. 9. (Color online) Parity plot of A_N, predicted by equation (21) vs. measured in every experiment during 0.042 (expressed in t_σ, so corresponding to 0.7 ms) after the rim detached from the substrate edge. The black line corresponds to A_N (th.) = A_N (exp.). Symbols (resp. colors) correspond to different We (resp. α_N), as described in table I (resp. II).
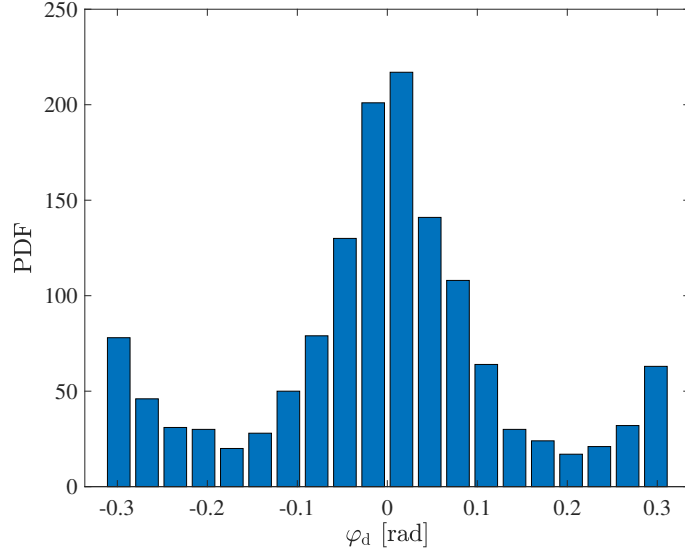

FIG. 10. Probability distribution function of the angular position φ_d of droplets at the moment of their ejection. The angle φ_d corresponds to θ_d calculated modulo $2\pi/N$ according to equation (2), thereby taking the substrate symmetry into account. Droplets from all experiments are pooled in this distribution.

V. EJECTED DROPLETS

The angular position φ_d at which the droplets are ejected is calculated modulo $2\pi/N$ according to equation (2) to take the substrate symmetry into account. The distribution of φ_d in which droplets from all experiments are pooled is represented in figure 10. Evidently, droplets are preferentially ejected at positions $\varphi_d = 0$ aligned with the troughs of the substrate edge. A secondary maximum of occurrence is observed in $\varphi_d = \pm\pi/N$, i.e., at positions aligned with the peaks of the substrate edge. Nevertheless, less droplets are ejected at $\phi_d \simeq \pm\pi/N$ than at $\phi_d \simeq 0$.

The velocity direction in which the droplets are ejected is represented by θ_v, namely the relative angle between the velocity vector and the radial direction at the position of ejection. The swarm chart of figure 11 indicates that most droplets ejected during the rim expansion ($\tau_d < 0.3$) are ejected radially, i.e., close to $|\theta_v| = 0$. Starting from $\tau_d \gtrsim 0.2$, a growing number of droplets are ejected in other, random directions.
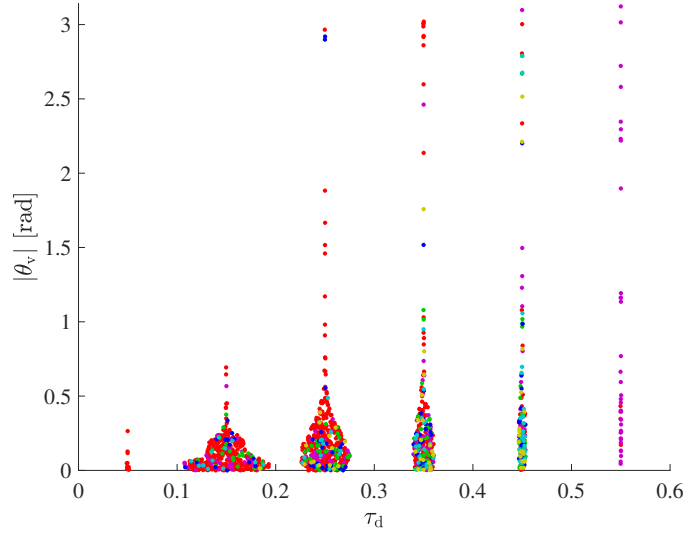
FIG. 11. (Color online) Swarm chart of the angle $|\theta_v|$ between the droplet velocity at ejection and the radial direction at angular position θ_d, as a function of ejection time τ_d. The swarm chart is a plot where data are binned (here at $\tau_d = 0.05$, 0.15, 0.25, etc.) then randomly scattered along the abscissa with an amplitude proportional to the density of data points around each value of $|\theta_v|$. The envelope of the data points therefore corresponds to the probability distribution of $|\theta_v|$ in a given bin of τ_d, similarly to a violin plot. Droplets from every experiment are pooled in this distribution, with colors corresponding to different α_N, according to table II.
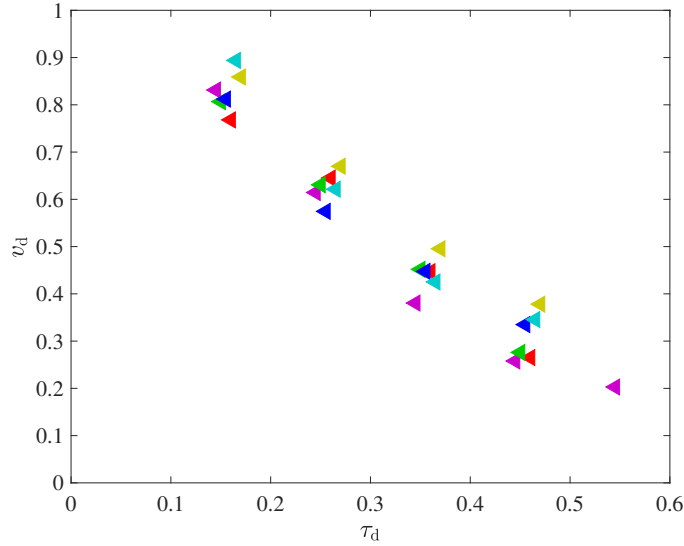
FIG. 12. (Color online) Average speed v_d (normalized by impact speed U) of droplets ejected at a given time τ_d (bins of ± 0.05), for the six experiments at We $= 1065$ and different values of α_N (colors, according to table II).

As seen in figure 12, the average droplet ejection speed v_d decreases with increasing time of ejection τ_d, as already observed for drop impacts on poles [24] and straight edges [11]. Interestingly, v_d is slightly larger for substrates with larger teeth (e.g., substrates 5 and 6 in table II).

Finally, figure 13 shows a swarm chart of the droplet volume Ω_d as a function of the ejection position φ_d. It proves that the largest droplets, corresponding to a volume higher than 0.5% of the impacting drop, are mostly ejected in directions aligned with troughs of the substrate edge.
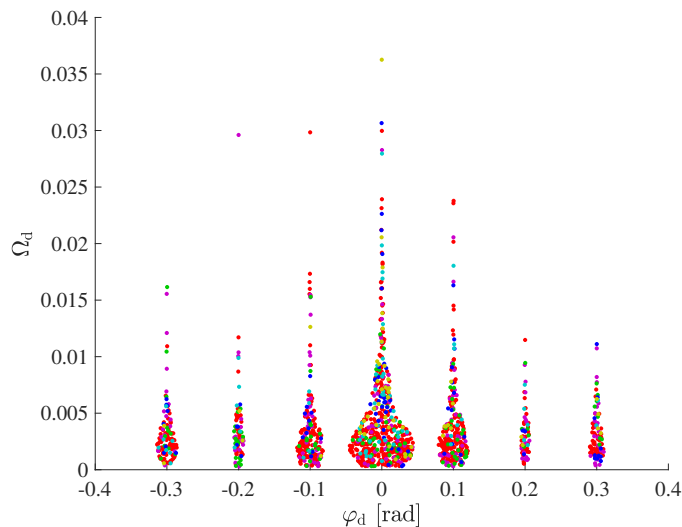
FIG. 13. (Color online) Swarm chart of the volume Ω_d of ejected droplets (normalized by the volume of the impacting drop), as a function of the angular position of ejection φ_d as defined in equation (2). The working principle of the swarm chart is recalled in the caption of figure 11. Droplets from every experiment are pooled in this distribution, with colors corresponding to different α_N, according to table II.

VI. CONCLUSION

This work investigated the dynamics of the sheet, rim and droplets formed when an impacting drop spreads beyond the edge of a solid substrate. It focused on the possible influence of the edge shape on this dynamics. In all the regimes explored in these experiments, the rim significantly deviated from axisymmetry during sheet expansion. It showed troughs (resp. peaks) in directions corresponding to edge peaks (resp. troughs). This corroborates previous observations on convex polygonal substrates [29]. It is intuitively explained by the fact that in edge peak directions, the liquid must spread longer on the substrate before reaching its edge, which comes with additional viscous dissipation and a reduced initial rim speed. Consistently, the shaping of the rim was marked more at larger viscosity.

We developed an analytical model of the rim deformation based on the hypothesis that in each direction, the rim expands independently of the other directions. The model provides a good prediction of the rim deformation at early times and correctly reproduces variations with the Weber number and the amplitude of edge teeth. As predicted, larger teeth result in a stronger shaping of the rim. A model that provides a prediction at later times would need to consider azimuthal interactions of rim and sheet, and it is left to future work.

The ejection of droplets from the rim responds to this modification of rim shape and dynamics. During the rim expansion ($\tau_\mathrm{d} < 0.3$), droplets are preferentially ejected in the directions corresponding to rim peaks (aka. edge troughs, $\varphi_\mathrm{d} \simeq 0$). They are mostly ejected radially ($\theta_\mathrm{v} \simeq 0$) and they are larger than droplets emitted in other directions. On average, droplets go slightly faster when edge teeth are present. It can therefore be concluded that the shape of a substrate edge may significantly influence the ejection of droplets emitted upon drop impact close to this edge. Droplets emitted during sheet and rim expansion are larger, faster, and ejected in preferential directions. As far as plant leaves are concerned, this mechanism certainly shapes, to some extent, the dispersal pattern of anything, from leached ions to spores, that could be transported in these droplets.
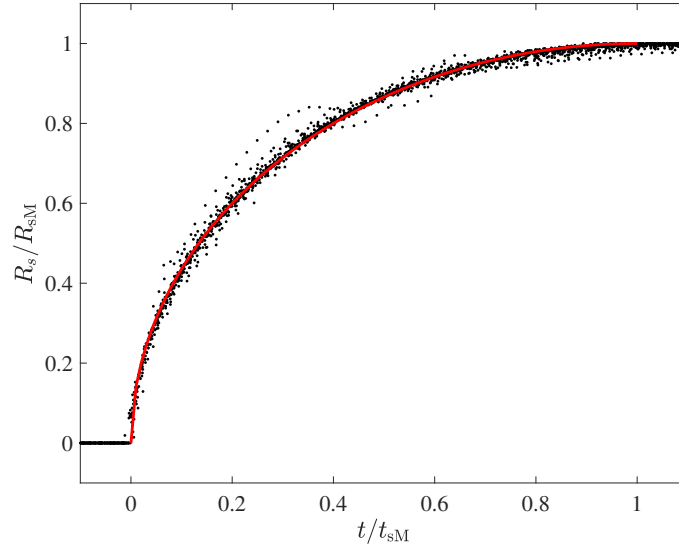
FIG. 14. (Color online) Time evolution of the rim radius $R_s(t)$ on an unbounded substrate. The rim radius is normalized by its maximum value R_{sM} and the time is normalized by the time t_{sM} that it takes to reach this radius. Black dots correspond to experimental data for drops made of various water/glycerol mixtures, impacting at different speeds. The red curve represents equation (A1).

Appendix A: Spreading on an unbounded substrate

Drops with the same diameter D as in the main experiments impacted a square horizontal plate of length 7.5 cm, i.e., significantly larger than the maximum spreading diameter of the drops. The spreading kinematics was recorded at a frame rate of 10000 fps, with a resolution of 62 μm/pix. Six different release heights (from 23 cm to 173 cm) were considered, which corresponded to impact velocities between 2 m/s and 5.4 m/s. Four mixtures of water and glycerol were considered too, with respective percentage of glycerol (in volume) of 0%, 25%, 40% and 55%. Densities and viscosities were obtained from an online calculator at www.met.reading.ac.uk, and surface tension was obtained from Takamura et al., J. Petroleum Sci. Eng. 98-99, 2012. The initial drop diameter D, the impact speed U and the time-evolution of the rim radius $R_s(t)$ were measured by image processing.

As seen in Fig. 14, the time evolution of the rim radius $R_s(t)$, once normalized, satisfies equation (10) with a unique function $F(T)$ which is very well approximated by

$$F(T) = \sqrt{T(2 - T)} \tag{A1}$$

as already shown for pure water drops in [12]. The factor involved in equation (21) is therefore

$$\frac{F''_{ae}}{F'_{ae}} = \frac{-1}{T_{ae}(1 - T_{ae})(2 - T_{ae})}. \tag{A2}$$

The maximum spreading radius R_{sM} is a function of We and Oh. Several approximations of this function were proposed in various works [35, 36, 38, 39]. As these approximations are only valid in specific ranges of We and Oh and possibly dependent on the wetting properties and roughness of the substrate, we determined our own approximation, valid in the range explored with our main data set:

$$R_{sM} \simeq 0.39 \left(\frac{\text{We}}{\text{Oh}} \right)^{1/5}. \tag{A3}$$

As seen in Figure 15, this equation is in very good agreement with the measurements of this maximum radius.

Figure 16 indicates that

$$t_{sM} \simeq 1.9 R_{sM} \text{We}^{-1/2}, \tag{A4}$$
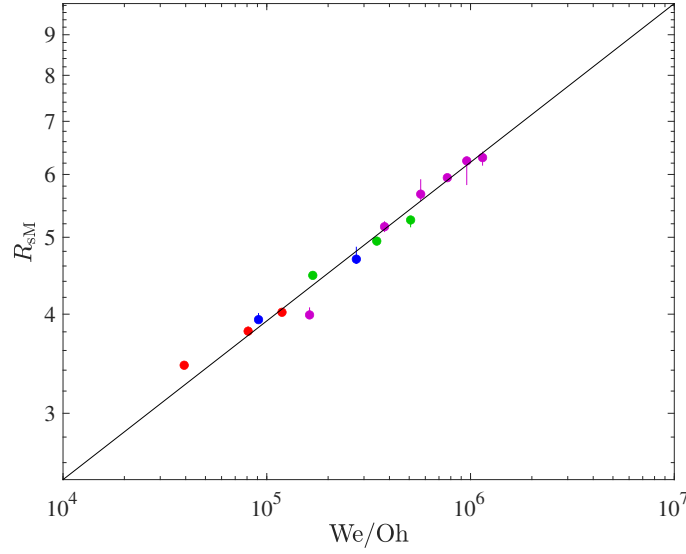
in agreement with the prediction of [39].

FIG. 15. (Color online) Maximum radius R_{sM} of the rim of a drop spreading on an unbounded substrate, as a function of We/Oh. Symbols with different colors correspond to experiments with different water-glycerol mixtures. The power law (black line) is given by equation (A3).
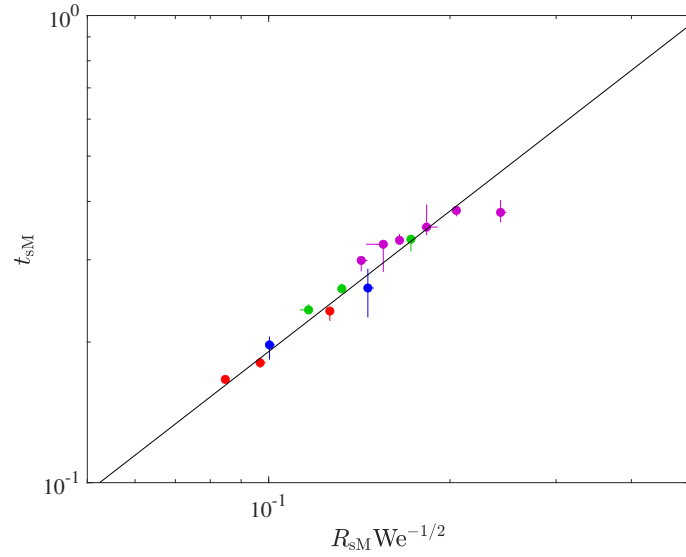

FIG. 16. (Color online) Time after impact t_{sM} at which the maximum radius R_{sM} of the rim is reached, as a function of $R_{\text{sM}}\text{We}^{-1/2}$. Symbols with different colors correspond to experiments with different water-glycerol mixtures. The black line represents equation (A4).

[1] D. F. Levia, K. Nanko, H. Amasaki, T. W. Giambelluca, N. I. S. Hotta, R. G. Mudd, M. A. Nullet, N. Sakai, Y. Shinohara, X. Sun, C. Tantasirin, and K. Yamada, Throughfall partitioning by trees, Hydrol. Process. **33**, 1698 (2019).

[2] A. Roth-Nebelsick, W. Konrad, M. Ebner, T. Miranda, S. Thielen, and J. H. Nebelsick, When rain collides with plants - patterns and forces of drop impact and how leaves respond to them, J. Exp. Biol. **73**, 1155 (2022).

[3] J. Marshall and W. M. Palmer, The distribution of raindrops with size, Journal of meteorology **5**, 165 (1948).

[4] D. F. Levia, S. A. Hudson, P. Llorens, and K. Nanko, Throughfall drop size distributions: a review and prospectus for future research, WIREs Water , 4:e1225 (2017).

[5] K. Nanko, S. Mizugakia, and Y. Onda, Estimation of soil splash detachment rates on the forest floor of an unmanaged japanese cypress plantation based on field measurements of throughfall drop sizes and velocities, Catena **72**, 348 (2008).

[6] K. Nanko, Y. Onda, A. Ito, S. Ito, S. Mizugaki, and H. Moriwaki, Variability of surface runoff generation and infiltration

rate under a tree canopy: indoor rainfall experiment using japanese cypress (chamaecyparis obtusa), Hydrol. Process. **24**, 567 (2010).

[7] J. Avelino, S. Vilchez, M. B. Segura-Escobar, M. A. Brenes-Loaiza, E. d. M. Virginio Filho, and F. Casanoves, Shade tree chloroleucon eurycyclum promotes coffee leaf rust by reducing uredospore wash-off by rain, Crop Protection **129**, 105038 (2020).

[8] L. Huber, H. A. McCartney, and B. D. L. Fitt, Influence of target characteristics on the amount of water splashed by impacting drops, Agricultural and Forest Meteorology **87**, 201 (1997).

[9] T. Gilet and L. Bourouiba, Fluid fragmentation shapes rain-induced foliar disease transmission, J. R. Soc. Interface **12**, 20141092 (2015).

[10] B. D. L. Fitt, H. A. McCartney, and P. J. Walklate, The role of rain in dispersal of pathogen inoculum, Annu. Rev. Phytopathol. **27**, 241 (1989).

[11] S. Lejeune, T. Gilet, and L. Bourouiba, Edge effect: Liquid sheet and droplets formed by drop impact close to an edge, Phys. Rev. Fluids **3**, 083601 (2018).

[12] S. Lejeune and T. Gilet, Drop impact close to the edge of an inclined substrate: Liquid sheet formation and breakup, Phys. Rev. Fluids **4**, 053601 (2019).

[13] Y. Wang and L. Bourouiba, Non-isolated drop impact on surfaces, J. Fluid Mech. **835**, 24 (2018).

[14] P. Tsai, M. H. W. Hendrix, R. R. M. Dijkstra, L. Shuib, and D. Lohse, Microscopic structure influencing macroscopic splash at high weber number, Soft Matter **7**, 11325 (2011).

[15] A. Rozhkov, B. Prunet-Foch, and M. Vignes-Adler, Impact of water drops on small targets, Phys. Fluids **14**, 3485 (2002).

[16] B. Néel, H. Lhuissier, and E. Villermaux, 'fines' from the collision of liquid rims, J. Fluid Mech. **893**, A16 (2020).

[17] E. Villermaux and B. Bossa, Drop fragmentation on impact, J. Fluid Mech. **668**, 412 (2011).

[18] Y. Wang and L. Bourouiba, Non-galilean taylor-culick law governs sheet dynamics in unsteady fragmentation, J. Fluid Mech. **969**, A19 (2023).

[19] S. Arora, C. Ligoure, and L. Ramos, Interplay between viscosity and elasticity in freely expanding liquid sheets, Physical Review Fluids **1**, 083302 (2016).

[20] M. Arogeti, E. Sher, and T. Bar-Kohany, Drop impact on small targets with different target-to-drop diameters ratio, Chem. Eng. Sci. **193**, 89 (2019).

[21] Y. Wang, R. Dandekar, N. Bustos, S. Poulain, and L. Bourouiba, Universal rim thickness in unsteady sheet fragmentation, Phys. Rev. Lett. **120**, 204503 (2018).

[22] R. Krechetnikov, Stability of liquid sheet edges, Phys. Fluids **22**, 092101 (2010).

[23] Y. Wang and L. Bourouiba, Growth and breakup of ligaments in unsteady fragmentation, J. Fluid Mech. **910**, A39 (2021).

[24] Y. Wang and L. Bourouiba, Unsteady sheet fragmentation: droplet sizes, J. Fluid Mech. **848**, 946 (2018).

[25] C. Vernay, L. Ramos, and C. Ligoure, Free radially expanding liquid sheet in air: Time-and space-resolved measurement of the thickness field, Journal of Fluid Mechanics **764**, 428 (2015).

[26] G. Lagubeau, M. A. Fontelos, C. Josserand, A. Maurel, V. Pagneux, and P. Petitjeans, Flower patterns in drop impact on thin liquid films, Phys. Rev. Lett. **105**, 184503 (2010).

[27] J. Parmentier, V. Terrapon, and T. Gilet, Drop impact on thin film: Mixing, thickness variations, and ejections, Phys. Rev. Fluids **8**, 053603 (2023).

[28] L. V. Zhang, P. Brunet, J. Eggers, and R. D. Deegan, Wavelength selection in the crown splash, Physics of Fluids **22**, 122105 (2010).

[29] G. Juarez, T. Gastopoulos, Y. Zhang, M. L. Siegel, and P. E. Arratia, Splash control of drop impacts with geometric targets, Physical Review E - Statistical, Nonlinear, and Soft Matter Physics **85**, 026319 (2012).

[30] A. Gauthier, S. Symon, C. Clanet, and D. Quéré, Water impacting on superhydrophobic macrotextures, Nat. Commun. **6**, 8001 (2015).

[31] A. Nasto, P.-T. Brun, and A. E. Hosoi, Drop impact on hairy surfaces, Phys. Rev. Fluids **4**, 064004 (2019).

[32] E. Dressaire, L. Courbin, A. Delancy, M. Roper, and H. A. Stone, Study of polygonal water bells: inertia-dominated thin-film flows over microtextured surfaces, J. Fluid Mech. **721**, 46 (2013).

[33] J. Parmentier, S. Lejeune, M. Maréchal, F. Bourges, D. Genty, V. Terrapon, J.-C. Maréchal, and T. Gilet, A drop does not fall in a straight line: a rationale for the width of stalagmites, Proc. R. Soc. A **475**, 20190556 (2019).

[34] E. J. Watson, The radial spread of a liquid jet over a horizontal plane, Journal of Fluid Mechanics **20**, 481–499 (1964).

[35] I. V. Roisman, R. Rioboo, and C. Tropea, Normal impact of a liquid drop on a dry surface: model for spreading and receding, Proceedings of the Royal Society A: Mathematical, Physical and Engineering Sciences **458**, 1411 (2002).

[36] C. Clanet, C. Beguin, D. Richard, and D. Quéré, Maximal deformation of an impacting drop, J. Fluid Mech. **517**, 199 (2004).

[37] I. V. Roisman, Inertia dominated drop collisions. ii. an analytical solution of the navier-stokes equations for a spreading viscous film, Physics of Fluids **21**, 052104 (2009).

[38] N. Laan, K. G. de Bruin, D. Bartolo, C. Josserand, and D. Bonn, Maximum diameter of impacting liquid droplets, Phys. Rev. Applied **2**, 044018 (2014).

[39] J. M. Gordillo, G. Riboux, and E. S. Quintero, A theory on the spreading of impacting droplets, J. Fluid Mech. **866**, 298 (2019).